LETTER TO THE EDITOR

The Missing Mechanism: Picoflare Heating in the Solar Corona

O. Podladchikova^{1,2}

¹ Igor Sikorsky Kyiv Polytechnic Institute, Peremohy Avenue 37, 03056 Kyiv, Ukraine

Leibniz Institute for Astrophysics Potsdam, An der Sternwarte 16, 14482 Potsdam, Germany e-mail: epodlad@gmail.com

Received 26 October 2025 / Accepted

ABSTRACT

The coronal heating problem has been explored through wave heating and impulsive nanoflare paradigms. Solar Orbiter observations reveal picoflares $(10^{20}-10^{24} \text{ erg})$ extending below the Parker–Aschwanden minimal coronal nanoflare limit. These events involve two distinct mechanisms: short-duration looptop tearing-mode reconnection and long-duration footpoint anomalous resistivity. This dualmechanism framework resolves the long-standing energy partition paradox and bridges photospheric energy injection with coronal

Key words. Sun: corona - Sun: UV radiation - Magnetic reconnection - Plasmas - Sun: magnetic fields - Magnetohydrodynamics

Received 26 October 2025 / Accepted

The coronal heating problem has been explored through wave heat reveal picoflares (10²⁰–10²⁴ erg) extending below the Parker–Asch distinct mechanisms: short-duration looptop tearing-mode reconne mechanism framework resolves the long-standing energy partition thermalization.

Key words. Sun: corona – Sun: UV radiation – Magnetic reconne (MHD)

1. Introduction

The million-degree solar corona represents one of the most enduring puzzles in astrophysics (Parker 1988). The required energy flux of ~ 3×10⁵ erg s⁻¹ cm⁻² for the quiet Sun (Withbroe & Noyes 1977) must be transported from the photosphere through the chromosphere and dissipated in the corona.

Two principal heating paradigms have dominated: wave heating and impulsive nanoflare heating. Wave heating operates effectively in long loops (> 50 Mm) and open field regions where Alfvén travel times permit sufficient wave dissipation (Heyvaerts & Priest 1983). Impulsive heating, following Parker (1988), operates through footpoint shuffling building magnetic stress that is released through reconnection.

However, both paradigms faced limitations. Wave models struggled to explain heating in short, low-lying loops, while nanoflare models could not account for the faintest energy releases. The fundamental work of Aschwanden (2000) established that traditional nanoflares have a natural lower limit around 10²⁴ erg, with rescaling to quiet-Sun conditions yielding ~ 10²³ erg. This created a theoretical barrier that seemed to prevent nanoflares from explaining the faintest coronal heating events. prevent nanoflares from explaining the faintest coronal heating events.

The recent Solar Orbiter observations have broken through this barrier. Podladchikova et al. (2025) performed the thermal energy analysis of campfires, revealing energies extending from 10²⁰ to 10²⁴ erg—fundamentally below the traditional nanoflare limit. This breakthrough was made possible by Solar Orbiter's unique capabilities: observations from 0.5 AU with unprecedented spatial resolution, combined with multi-volume modeling and robust detection thresholds. These picoflare observations complete our understanding of coronal heating by revealing previously invisible energy release mechanisms.

2. Observational Basis: Two Populations of **Picoflares**

The discovery of "campfires" by Berghmans et al. (2021) represents a critical advance in solar physics for several key reasons. First, using Solar Orbiter's EUI instrument from 0.5 AU, they achieved the first morphological resolution of these small-scale events (picoflares), moving beyond the statistical inference that was possible with previous SOHO/EIT data from 1 AU, which could only detect unresolved brightenings. The direct observation of their structure and temporal behavior suggests that campfires constitute a new phenomenological class, qualitatively distinct from the more impulsive nanoflare concept. Consequently, this direct observation challenges existing coronal heating models and formulates new, unresolved questions about the role of these ubiquitous events.

The work of Zhukov et al. (2021) represented another fundamental advancement: for the first time, it was possible to calculate precise vertical heights of these energy release events using high-resolution stereoscopy. Solar Orbiter's unique orbital dynamics, positioned 31.5° west of Earth and observing from 0.5 AU, enabled triangulation of the same events observed simultaneously by SDO/AIA. This technological breakthrough allowed exact determination of which atmospheric layer hosted each event, with specific plasma β and other plasma properties that favor particular dissipation mechanisms. The combination of observations from two different vantage points, together with the unprecedented resolution from 0.5 AU, made this understanding possible.

Podladchikova et al. (2025) provided a detailed energy analysis of campfires, completing this picture. By implementing multiple geometrical volume models and rigorous uncertainty quantification, they demonstrated that thermal energies of these events span the picoflare range $(3 \times 10^{20} \text{ to } 1 \times 10^{24} \text{ erg})$, with occurrence rates of $3 \times 10^{-20} \text{ s}^{-1} \text{ cm}^{-2}$ for events above the 3σ threshold. This energy estimation was made possible by:

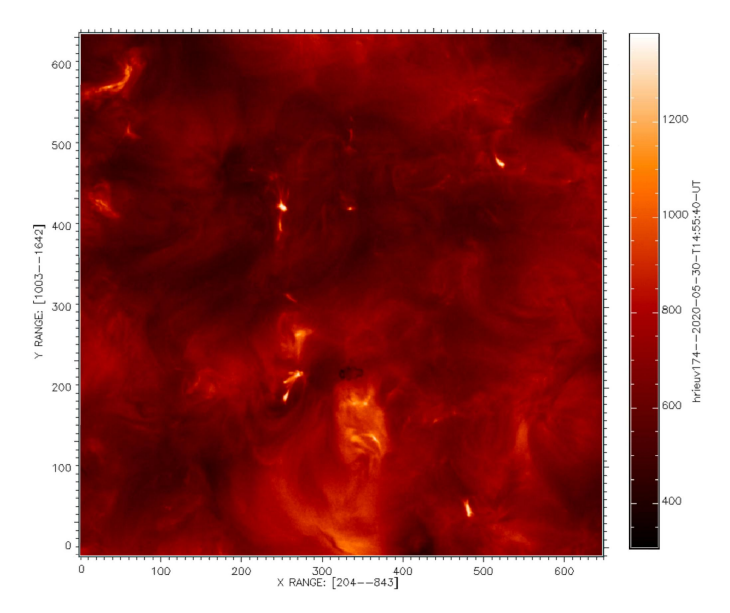


Fig. 1. The quiet-Sun corona as seen by Solar Orbiter/EUI, revealing the resolved structure of "campfires" (Berghmans et al. 2021). These impulsive brightenings are fundamental drivers of coronal heating. See the supplementary Movie.

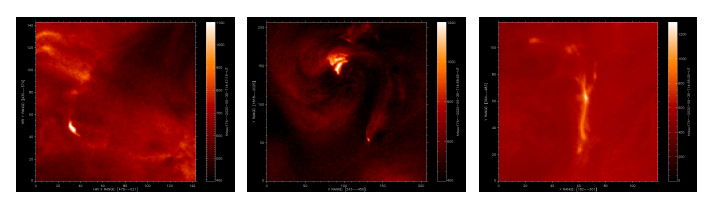


Fig. 2. Picoflare events resolved by Solar Orbiter/EUI from 0.5 AU, confirming what was inferred statistically (Benz & Krucker 1998; Aschwanden 2000). (Left) Population A: looptop brightening from tearing-mode reconnection $(3.2 \times 10^{23} \text{ erg})$ (Looptop Event). (Middle) Population B: footpoint heating from anomalous resistivity $(1.7 \times 10^{22} \text{ erg})$ (Footpoint Event). (Right) Coupled A-B Event: Looptop reconnection driving footpoint dissipation (Coupled Event).

- High spatial resolution from 0.5 AU (198 km per pixel)
- Multi-volume modeling approach (elliptical loop and cube models)
- Robust detection methodology with $\geq 3\sigma$ and $\geq 5\sigma$ thresholds
- Large statistical sample (12,107 events for $\geq 3\sigma$ threshold)
- DEM analysis for temperature and density determination

This comprehensive approach allowed, for the first time, reliable estimation of energies fundamentally below the traditional nanoflare limit.

The visual inspection and subsequent analysis revealed that of 12,107 events shows a clear bimodal distribution, as illustrated in Figure 3. This bimodality resolves a fundamental paradox in coronal heating: rather than a single population of events, we observe two distinct populations operating through different physical mechanisms in different atmospheric layers.

2.1. Population A: Looptop Events

Population A events (Figure 2, left) are characterized by:

- Duration: 1–10 seconds (Alfvénic timescales)
- Location: Looptops, 2.5-5 Mm altitude
- Temperature: 1.3–1.5 MK (hotter than background)

- Energy: 10²²-10²⁴ erg

- Mechanism: Tearing-mode reconnection of perpendicular

- Characteristic: Rapid, impulsive brightenings

2.2. Population B: Footpoint Events

Population B events (Figure 2, middle) show:

- Duration: 10–100 seconds (resistive timescales)

- Location: Footpoints, 1-2.5 Mm altitude

- Temperature: 1.0–1.2 MK (slightly above background)

- Energy: 10^{20} - 10^{22} erg

- Mechanism: Anomalous resistivity of parallel currents

- Characteristic: Gradual, sustained heating

Stereoscopic height measurements by Zhukov et al. (2021) provide important evidence for this spatial separation. The footpoint events (Population B) concentrate below 2.5 Mm, near the transition region boundary (typically located around 2000 km above the photosphere), while looptop events (Population A) occur higher in the corona at 2.5–5 Mm. This precise height discrimination was only possible through Solar Orbiter's unique vantage point and simultaneous observations with SDO/AIA.

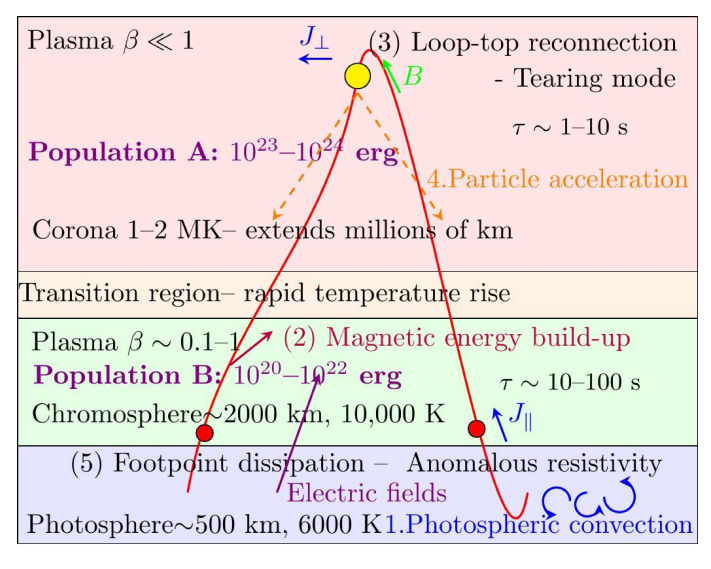


Fig. 3. Schematic of atmospheric energy transfer: photospheric twisting (1-2) leads to loop-top reconnection (3, Population A) and footpoint heating (4-5, Population B), with characteristic timescales.

The detailed energy analysis by Podladchikova et al. (2025) established picoflares as a distinct energy class below traditional nanoflares. Their power-law distributions (with exponents of $\alpha=2.32$ for $\geq 5\sigma$ events and $\alpha=2.82$ for $\geq 3\sigma$ events) were found to extend over three orders of magnitude in energy. It is important to note, however, that a more precise determination of these slopes requires further investigation, as their values can depend on observing conditions and instrumental capabilities. This variability is well-documented in studies of nanoflares, which show a broad range of power-law indices. One can cautiously conclude that the derived slopes for picoflares are broadly similar to those found for nanoflares, typically clustering around a value of 2.

3. Theoretical Framework: From Parker's Nanoflares to Picoflares

3.1. Parker's Nanoflare Model and Its Limitations

Parker (1988) estimated nanoflare energy for active regions:

$$E_{\text{Parker,AR}} \approx \frac{B^2}{8\pi} V \approx \frac{(100 \text{ G})^2}{8\pi} (10^{24} \text{ cm}^3) \approx 10^{24} \text{ erg}$$

This model assumed twisted loops with perpendicular currents dissipating through reconnection, valid in regions where plasma $\beta < 1$ and sufficiently above the chromosphere to form stable current sheets.

3.2. Aschwanden's Scaling and the Coronal Nanoflare Limit

Aschwanden (2000) performed detailed scaling of nanoflare energies based on observed parameters from TRACE and SOHO/EIT. Building on the foundational work of Golub et al. (1980) who established the relationship between magnetic field strength and coronal heating, Aschwanden derived the minimal observable energy for a coronal nanoflare:

$$E_{\text{nano}} \approx 3n_e k_B T V \approx 3 \times (10^9 \text{ cm}^{-3}) \times (1.38 \times 10^{-16} \text{ erg K}^{-1})$$

 $\times (10^6 \text{ K}) \times (10^{24} \text{ cm}^3) \approx 4 \times 10^{24} \text{ erg}$

This analysis confirmed that traditional coronal nanoflares cannot extend below $\sim 10^{24}$ erg. Rescaling for quiet-Sun conditions:

$$E_{\text{Parker,QS}} \approx \frac{(10 \text{ G})^2}{8\pi} (3 \times 10^{19} \text{ cm}^3) \approx 1.2 \times 10^{23} \text{ erg}$$

This represents the natural limit for Parker-type nanoflares and explains Population A events, but cannot account for the numerous lower-energy Population B events.

Klimchuk (2006, 2015) further developed this framework, emphasizing that nanoflares must be understood as coronal events involving current dissipation in the low- β plasma above the chromosphere. Their work showed that the observed statistics of larger flares could be extrapolated to the nanoflare regime, but always with a lower limit around 10^{24} erg for coronal events.

3.3. The Priest School: Tearing-Mode Instability and Current Sheet Formation

The Parker framework was rigorously developed by Priest et al. (1998); Priest & Forbes (2000) and subsequent work, providing detailed mathematical treatment of current sheet formation and dissipation. The Priest school demonstrated that:

- Footpoint shuffling naturally leads to current sheet formation through topological dissipation
- Tearing-mode instabilities develop in perpendicular current sheets, with growth rate: $\gamma_{\text{tearing}} \approx \frac{V_A}{L} S^{-1/2} \left(\frac{\lambda}{L}\right)^{-3/2}$, where $S = \frac{LV_A}{\eta}$ is the Lundquist number, λ is the wavelength, and η is the magnetic diffusivity
- Magnetic islands form during the nonlinear phase of tearingmode instability, enhancing energy release
- Reconnection occurs on Alfvénic timescales ($\tau_A \approx L/V_A$)
- This process requires plasma β < 1 and operates best in the corona proper above 2 Mm

Browning & Van der Linden (2003) provided numerical evidence, showing that slow footpoint twisting drives coronal loops to kink-instability thresholds, triggering nanoflare-like reconnection events. This mechanism naturally produces energy releases in the 10^{23} – 10^{25} erg range with timescales of 1–10 seconds, perfectly matching Population A observations.

However, these models still could not explain events below 10^{23} erg, as they focused exclusively on perpendicular current dissipation in the coronal part of loops.

3.4. Anomalous Resistivity: The Missing Mechanism for Low-Energy Picoflares

The resolution lies in recognizing that Population B events represent parallel current dissipation in the low- β environment of footpoint regions. In the low chromosphere and transition region, energy transfer starts through parallel electric fields or quasiparallel currents. When current density exceeds critical thresholds, two primary instabilities drive anomalous resistivity in the collisionless plasma:

- **Buneman instability**: Occurs when electron drift velocity exceeds electron thermal velocity ($v_d > v_{th.e}$)
- Ion-acoustic instability: Occurs when $v_d > c_s$ (ion sound speed)

In collisionless plasma conditions typical of the low corona, Spitzer conductivity fails because particle collisions are insufficient. Instead, heating occurs through exchange of momentum and energy between ions and electrons via wave-particle interactions. These mechanisms are well-studied in plasma physics and are known to operate effectively under low-corona conditions.

The critical current density for instability onset is:

$$j > n_e e c_s$$

where $c_s = \sqrt{k_B T_e/m_i} \approx 50$ km/s is the ion sound speed. When exceeded, anomalous resistivity enhances dissipation by 3–5 orders of magnitude. For typical quiet-Sun parameters ($n_e \approx 10^9$ cm⁻³, $L \approx 1000$ km, $w \approx 200$ km):

$$E_{\text{anomalous}} \approx 10^{20} - 10^{22} \text{ erg}$$

The characteristic timescale is resistive and sound-speed limited: $\tau_{\parallel} \approx L/c_s \approx 10\text{--}100 \text{ s}$

This perfectly matches Population B observations and explains why these events concentrate in footpoint regions where parallel currents dominate.

3.4.1. Reconnection-Generated Electric Fields and Footpoint Heating

Magnetic reconnection generates potential differences that drive currents toward footpoints. The efficiency of particle acceleration depends on the reconnection geometry:

Single-loop tearing-mode reconnection creates modest potentials:

$$\Delta\Phi \approx v_{\rm rec}BL_{\rm sheet} \approx (3 \text{ km/s})(10^{-3} \text{ T})(10^6 \text{ m}) \approx 300 \text{ V}$$

producing limited particle acceleration.

– Reconnection between sheared magnetic loops generates stronger potentials $\Delta\Phi \sim 3$ kV through larger magnetic shear differences, driving more efficient particle acceleration.

These potentials drive parallel currents that become concentrated in the transition region. The current density in the coronal

$$j_{\parallel} = \sigma \frac{\Delta \Phi}{L} \approx 1.3 \times 10^{-3} \text{ A m}^{-2}$$

In the transition region, current channeling enhances densities by 3-4 orders of magnitude, reaching the critical threshold for anomalous resistivity:

$$j_{\text{crit}} = n_e e c_s \approx (10^{15} \text{ m}^{-3})(1.6 \times 10^{-19} \text{ C})(5 \times 10^4 \text{ m/s}) \approx 8 \text{ A m}^{-2}$$

The resulting energy release in footpoint volumes produces Population B events:

$$E \approx \eta_{\text{anom}} j^2 V \tau \approx 6 \times 10^{21} \text{ erg}$$

Such stochastic acceleration by DC electric fields has been extensively studied in the context of solar flares (Anastasiadis et al. 1997), and similar mechanisms may operate at the picoflare scale.

3.4.2. Chromospheric Electric Field Transport Mechanisms

Electric fields facilitate energy transfer through the chromospheric barrier via: direct acceleration from photospheric motions generating $\mathbf{E} = -\mathbf{v} \times \mathbf{B}$; current channel formation via flux tube squeezing enhancing $j_{\parallel} \approx B/\mu_0 R_c$; and non-ideal MHD effects: ambipolar diffusion in partially ionized plasma creates additional electric fields: $\mathbf{E} = \eta \mathbf{j} + \eta_A (\mathbf{j} \times \mathbf{B}) \times \mathbf{B}/B^2$.

These mechanisms can overcome chromospheric radiative losses by maintaining current continuity, enabling rapid energy transfer, and explaining observed photosphere-corona correla-

This electric field mediated transport complements our dualmechanism model by explaining how energy bypasses the chromospheric radiative losses and directly powers both Population A (through current sheet formation) and Population B (through parallel electric fields) events. The characteristic properties of these two dissipation mechanisms are summarized in Table 1.

Table 1. Characteristic scales and times for picoflare dissipation.

Parameter	Tearing-mode Rec.	Anomalous Resistivity
Location ab. ph-re	Looptops (2.5–5 Mm)	Footpoints (1–2.5 Mm)
Current type	Perpendicular	Parallel
Trigger condition	Magnetic shear	$j > n_e e c_s$
Critical current	_	$j_{\rm crit} = n_e e c_s \approx 8 \text{ A m}^{-2}$
Instability	Tearing-mode	Buneman/ion-acoustic
Timescale	$\tau_A \approx L/V_A \approx 1-10 \text{ s}$	$\tau \approx L/c_s \approx 10$ –100 s
Energy scale	10^{23} – 10^{24} erg	10^{20} – 10^{22} erg
Spatial scale	Cur. sheet: 10–100 m	Cur. channel: 0.1-1 km
Plasma β	≪ 1	0.1-1
Heating mechanism	Magnetic reconnection	Wave-part. inter-tions

4. Conclusion

Solar Orbiter's unique observational capabilities-high-resolution imaging from 0.5 AU combined with stereoscopic triangulationhave fundamentally advanced our understanding of coronal heating. The mission has revealed that the corona is heated through two distinct but complementary mechanisms operating across different energy scales and spatial locations.

The comprehensive energy analysis by Podladchikova et al. (2025) demonstrates that picoflares follow a power-law distribution with slope $\alpha = 2.\overline{3}$, causing the total energy flux $F \propto$ $\int E^{1-\alpha} dE$ to converge at the lower limit. This indicates that numerous small-scale events dominate the heating budget, requiring a minimum energy of $E_{\rm min} \approx 1.25 \times 10^{18}$ erg to sustain the quiet-Sun heating flux, confirming theoretical predictions by Vlahos (1994) and Georgoulis & Vlahos (1996). However, this conclusion is sensitive to the exact slope value—a shallower slope ($\alpha = 1.9$) would shift energy dominance to larger nanoflares, highlighting the critical need for precise measurements.

Our unified framework resolves the long-standing debate between Aschwanden et al. (2017) and Benz (2017) regarding EUV nanoflare locations by demonstrating distinct mechanisms for different atmospheric regions:

- Loop tops: Tearing-mode reconnection drives nanoflares (> 10²⁴ erg)
- Footpoints: Anomalous resistivity powers picoflares (10²⁰- $10^{22} \, erg$
- Intermediate events: Mixed-characteristic events (10²²- 10^{24} erg) connect these regimes

The electric field serves as the fundamental mediator, transferring energy from reconnection sites at looptops to dissipation sites at footpoints, completing the energy cycle from photospheric motions to coronal thermalization.

The convergence of three key advances—morphological resolution of campfires (Berghmans et al. 2021), stereoscopic height determination (Zhukov et al. 2021), and comprehensive energy analysis (Podladchikova et al. 2025)—provides compelling evidence for this dual-mechanism model. Solar Orbiter's direct observations finally resolve the long-standing controversy about EUV nanoflare locations, confirming that both footpoint and looptop heating contribute significantly to the coronal energy budget. Future Solar Orbiter observations at 0.3 AU will further test this framework through direct resolution of current sheets and current densities, potentially revealing the fundamental building blocks of coronal heating.

References

```
Anastasiadis, A., Vlahos, L., & Georgoulis, M. K. 1997, The Astrophysical Jour-
nal, 489, 367
Aschwanden, M. J. 2000, The Astrophysical Journal, 531, 1127
Aschwanden, M. J., Caspi, A., Cohen, C. M. S., et al. 2017, ApJ, 836, 17
Benz, A. O. 2017, Living Reviews in Solar Physics, 14, 2
Benz, A. O. & Krucker, S. 1998, Solar Physics, 182, 349
Berghmans, D., Auchere, F., Long, D. M., & et al. 2021, Astronomy & Astro-
```

physics, 656, L4 Browning, P. K. & Van der Linden, R. A. M. 2003, Astronomy & Astrophysics,

400, 355 Georgoulis, M. K. & Vlahos, L. 1996, The Astrophysical Journal Letters, 469,

Golub, L., Maxson, C., Rosner, R., Serio, S., & Vaiana, G. S. 1980, The Astro-

physical Journal, 238, 343 Heyvaerts, J. & Priest, E. R. 1983, Astronomy and Astrophysics, 117, 220 Klimchuk, J. A. 2006, Solar Physics, 234, 41 Klimchuk, J. A. 2015, Philosophical Transactions of the Royal Society A, 373,

20140256 Parker, E. N. 1988, The Astrophysical Journal, 330, 474 Podladchikova, O., Warmuth, A., Harra, L., & et al. 2025, Astronomy & Astro-

physics, arXiv:2510.10340
Priest, E. R., Foley, C. R., Heyvaerts, J., & et al. 1998, Nature, 393, 545
Priest, E. R. & Forbes, T. G. 2000, Cambridge University Press
Vlahos, L. 1994, Space Science Reviews, 68, 39
Withbroe, G. L. & Noyes, R. W. 1977, Annual Review of Astronomy and Astro-

physics, 15, 363 Zhukov, A., Mierla, M., Auchere, F., & et al. 2021, Astronomy & Astrophysics, 656, A35

Acknowledgements. This work utilizes data from the Solar Orbiter mission.